ADVANCED QUANTUM TECHNOLOGIES
www.advquantumtech.com

Dynamic Continuous Variable Quantum Key Distribution for Securing a Future Global Quantum Network

Mikhael T. Sayat, Sebastian P. Kish, Ping Koy Lam, Nicholas J. Rattenbury, and John E. Cater*

Continuous variable quantum key distribution (CVQKD) is a developing method to secure information exchange in future quantum networks. With the recent developments in quantum technology and greater access to space, a global quantum network secured by CVQKD can be within reach. In this work, the structures of existing QKD networks are analyzed, and how they can be fit into a general overarching three-layer QKD network architecture for the endeavor of a global QKD network. Such a network can comprise different links in fiber and free-space. The finite size limit secret key rates (SKRs) with multidimensional reconciliation are calculated for the different links for which CVQKD can be used in such a network. The results show that CVQKD generally achieves longer distances and larger SKRs in inter-satellite, satellite-to-ground, fiber, and underwater links in descending order. The different links and nodes are classified and secret key distribution is studied as a graph problem. The link capacity, a routing metric for secret key distribution, which considers a dynamic SKR based on dynamic links is presented. Its use in simulated CVQKD networks is presented for the aim of spatiotemporal secret key distribution through a dynamic CVQKD network.

1. Introduction

Recent developments in quantum technology and access to space positions the development of a global quantum network within reach.[1] A nascent yet promising method of securing such a network is through continuous variable quantum key distribution (CVQKD). CVQKD uses the continuous amplitude and phase quadrature of light to encode a secret key between communicating parties which is then used to encrypt information.[2] Compared to the more established discrete variable QKD (DVQKD), CVQKD offers higher key rates, cheaper detection methods, and is more integrable with existing optical telecommunication networks.[2] In addition, CVQKD outperforms (DVQKD) in communicating channels with lower phase noise, and it is more robust against thermal noise.[3] The governing performance metric used is the secret key rate (SKR), which represents the size of the secret key that can be shared between communicating parties over time.

Many existing national QKD networks exist with different architectures, sizes, protocols, and achievable SKRs.[4] The first QKD network was the DARPA quantum network, which used the BB84 DVQKD protocol and achieved a SKR of 1 kbits^{-1}.[5,6] The Tokyo quantum network consists of six nodes using the decoy state BB84, DPS-QKD, BBM92, and SARG04 DVQKD protocols with a maximum SKR of 304 kbits^{-1}.[7,8] The SECOQC quantum network exhibits both CVQKD and DVQKD protocols utilizing both fiber and free-space channels and achieved a maximum SKR of 17 kbits^{-1}.[9,10] The Madrid quantum network was the first network to be integrated with an existing telecommunication network

M. T. Sayat, P. K. Lam
Quantum Innovation Centre (Q.InC)
Agency for Science Technology and Research (A*STAR)
2 Fusionopolis Way, Innovis #08-03, Singapore 138634, Republic of Singapore
E-mail: mikhael_sayat@imre.a-star.edu.sg

M. T. Sayat, N. J. Rattenbury
Department of Physics, Faculty of Science
University of Auckland
Auckland 1010, New Zealand

The ORCID identification number(s) for the author(s) of this article can be found under https://doi.org/10.1002/qute.202500135

DOI: 10.1002/qute.202500135

M. T. Sayat, P. K. Lam
Institute of Materials Research and Engineering (IMRE)
Agency for Science Technology and Research (A*STAR)
2 Fusionopolis Way, Innovis #08-03, Singapore 138634, Republic of Singapore

S. P. Kish
Data61
Commonwealth Scientific and Industrial Research Organisation
Marsfield, Sydney, NSW 2122, Australia

P. K. Lam
ARC Centre for Quantum Computation and Communication Technology, Research School of Physics
Australian National University
Canberra, ACT 2601, Australia

J. E. Cater
Department of Mechanical Engineering
University of Canterbury
Christchurch 8041, New Zealand

Table 1. Features of Existing QKD Networks.

QKD Network	Channels	Implementation	#Nodes	Max SKR	Protocol	Special Features
DARPA Quantum Network[5,6]	Fiber, Free-Space	Optical Switching, Trusted Relay	10	10 kbit/s	DVQKD	First QKD Network
Tokyo QKD Network[7]	Fiber	Trusted Relay	6	304 kbit/s	DVQKD	
SECOQC Quantum Network[9,10]	Fiber, Free-Space	Trusted Relay	6	17 kbit/s	CVQKD, DVQKD	QKD with Micius Satellite
Cambridge Quantum Network[19]	Fiber	Trusted Relay	3	2.58 Mbit/s	DVQKD	
Bristol Quantum Network[20,21]	Fiber	Untrusted Relay, SDN	8	83.9 kbit/s	DVQKD	SDN Implementation
Madrid Quantum Network[11,12]	Fiber	Optical Switching, Trusted Relay, SDN	12	70 kbit/s	CVQKD, DVQKD	First SDN QKD Network Integrated with Existing Telecom Network
Chinese Quantum Network[4,15]	Fiber, Free-Space	Optical Switching, Trusted Relay, Untrusted Relay	166	235 kbit/s	CVQKD, DVQKD	Largest QKD Network and is Integrated with Space

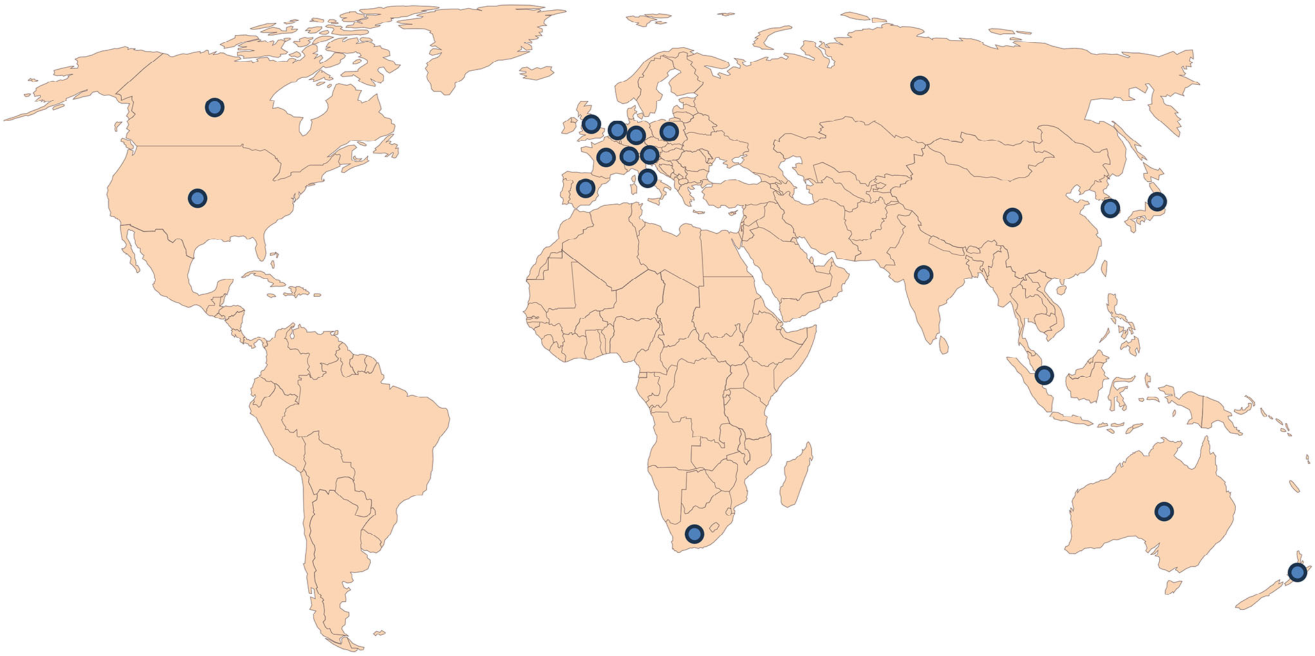

Figure 1. Locations of existing QKD networks, testbeds, demonstrations, and developments.[4,22–24]

and used a software-defined network (SDN) architecture, which replaced the traditional point-to-point architecture of other networks allowing for easier integration.[11–13] The SDN architecture controls the whole network as a whole as opposed to point-to-point, which controls individual links.[14] The Chinese quantum network is the largest existing network, which consists of 166 nodes in fiber and free-space using both CVQKD and DVQKD protocols with a maximum achievable SKR of 235 kbits^{-1}.[15] It includes Micius, the first quantum satellite, which achieved BB84 encryption between China and Vienna with a sifted key rate of 3 to 9 kbit/s over a satellite-to-ground link distance of 1000 to 600 km, respectively.[16] In addition, China demonstrated the first experimental demonstration of CVQKD using Einstein-Podolsky-Rosen entangled states, achieving 84 kbits^{-1} for an 80% transmission efficiency where the demonstrated scheme can be used for CVQKD networks.[17] A hybrid quantum QKD network was also proposed where CVQKD is used within metropolitan networks and DVQKD is used to connect these networks, along with the use of measurement device independent QKD systems, utilizing the advantages found in both CVQKD and DVQKD.[18]

Existing networks are predominantly based in fiber and use DVQKD protocols (a summary of significant QKD networks can be found in **Table 1** and locations of network developments is shown in **Figure 1**). However, it is beneficial to include CVQKD for its advantages and free-space links for spatial diversity. In establishing a secured global quantum network, it is beneficial to be

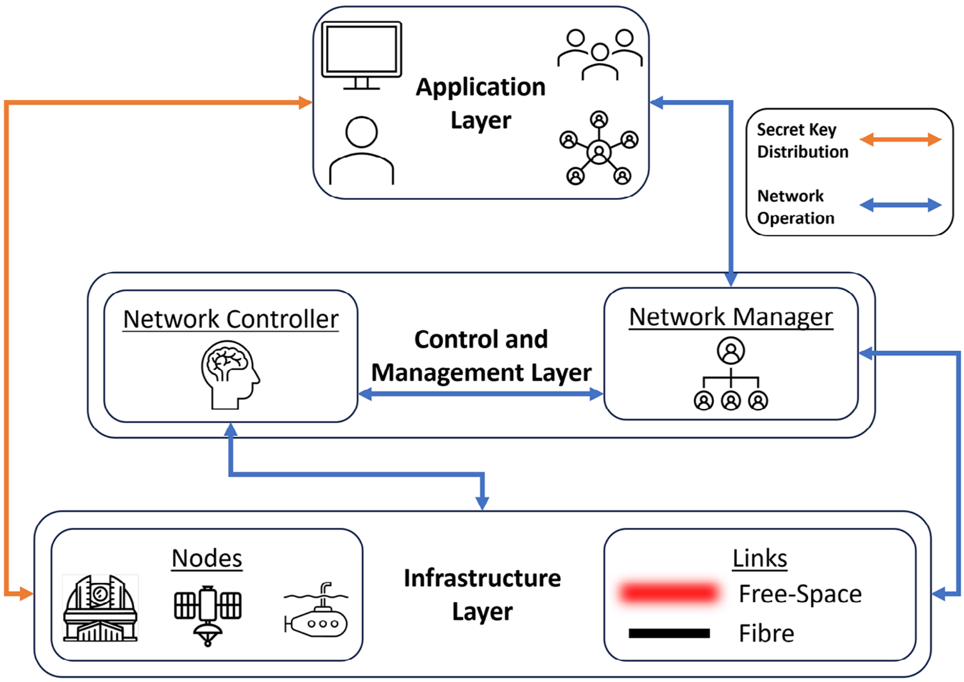

Figure 2. General architecture of a QKD network, consisting of the infrastructure layer (nodes, links, QKD-related devices), control and management layer (network controller and manager), and application layer (users).[25]

able to use available nodes and links from existing networks for both fiber and free-space QKD. This provides interconnectedness and spatiotemporal diversity whereby the transfer of secret keys can be performed through favorable channels in a dynamic network.

In this paper, we discuss how existing networks can be integrated into an overarching global quantum network architecture. In addition, we collectively present existing models for the feasibility of CVQKD through fiber and available free-space channels, which are then used to simulate CVQKD through a dynamic network. Here, we present the link capacity, which is dependent on a dynamic SKR and can be used as a routing metric to choose the optimum pathway in such a network.

2. Integrating QKD Networks

Multiple QKD networks can be connected into one overarching network architecture, such as that shown in **Figure 2**, which comprises of three layers.[25] The infrastructure layer consists of all the nodes, links between nodes, and any QKD-related devices required for the distribution and storing of secret keys. The control and management layer consists of the network controller and network manager. The network controller calibrates and controls the activation of nodes, and the link connections between them, for QKD operation. The network manager monitors the QKD nodes and links, keeping track of secret key and channel parameters, as well as supervising the network controller's calibration and activation of the infrastructure layer.

The application layer represents the end-users of QKD who require a secret key. Users request secret keys from the network manager, which then queries a corresponding node for a secret key. Once a secret key is available, the network manager instructs the network controller to activate the corresponding node to send the secret key to the user. It should be noted that the control and management layer exists only to activate, calibrate, and monitor the infrastructure layer. The distribution of secret keys occurs between the nodes and the application layer where the contents of the secret key remain undisclosed to the control and management layer.

In constructing a global quantum network, different national networks may need to adhere to a global QKD network architecture such as that shown in Figure 2. Operations and layer structures would need to be made compatible. The use of an SDN controller would allow easier integration, as demonstrated by the Madrid quantum network.[11]

Using the general three-layer QKD network architecture, the infrastructure layer would consist of the

- Nodes: optical ground stations (OGSs), satellites, submarines, high-altitude platforms, and
- Links: fiber, satellite-to-ground, submarine-to-ground, satellite-to-submarine, inter-satellite, inter-submarine.

The network manager in the control and management layer would monitor the channel parameters (transmittance, excess noise) based on the environment conditions inherent to each link e.g. visibility, refractive index structure parameter, chlorophyll concentration, link distances etc.

Although a general QKD network could consist of the three aforementioned layers (Figure 2), other networks (proposals and experimental) have adopted four layers,[26–31] five layers,[15] and six layers.[32] The additional layers arise from further division of the three general layers (infrastructure, control, and management, and application). If a global quantum network used the

Table 2. QKD Networks in the Three Layer General Network Architecture.

	General Network Architecture Layer		
	Application Layer	Control and Management Layer	Infrastructure Layer
DARPA Quantum Network[33]	Internet Key Exchange Daemon	Quantum Protocol Daemon, Optical Process Control	Physical Layer (Tx/Rx)
Tokyo QKD Network[7]	Communication Layer	Key Management Layer	Quantum Layer
SECOQC QKD Network[10]	Data Plane	Secret's Plane	Quantum Plane
Cambridge Quantum Network[19]	Application Layer	Network Key Delivery Layer	Quantum Layer
Bristol Quantum Network[20]		SDN Plane	Data Plane
Madrid Quantum Network[12]		SDN	
Chinese Quantum Network[15]	Application Layer	Classical Logical Layer, Classical Physical Layer, Quantum Logical Layer	Quantum Physical Layer

general three-layer QKD network architecture, the different number of layers in existing QKD networks[4] would need to be integrated into and made compatible with the three layers. **Table 2** shows the different layers of existing QKD networks and where they fit into the general three-layer architecture.

3. Secret Key Rate

CVQKD protocols can be classified into Gaussian modulated (GM)[2] or discrete modulated (DM) protocols.[34–36] In GM-CVQKD, the modulated coherent states follow a continuous Gaussian distribution in the amplitude and phase quadrature,[2] whereas DM-CVQKD have fixed modulations.[34–36] Although DM-CVQKD allows for large SKRs in low SNR regimes, security proofs are still an active field of research and currently less general than those in GM-CVQKD.[35,37–39] Due to the maturity of GM-CVQKD with well-established security proofs and higher SKRs with recent error correction codes,[40,41] it is the protocol used for SKR analysis in this work.

The secret key rate in the asymptotic limit, which assumes that an infinite number of symbols are sent, can be defined as:[2,35]

$$\mathrm{SKR}_{\mathrm{asy}} = \beta I_{AB} - S_{BE} \tag{1}$$

where β is the reconciliation efficiency based on the information reconciliation step during classical post processing. I_{AB} is the mutual information between Alice and Bob, and is the maximum amount of information that can be shared depending on the protocol and channel parameters. S_{BE} is the estimated upper bound on the information about the key known by Eve, and is known as the "Holevo Bound". Since S_{BE} is an upper bound, Equation (1) is the lower bound on the SKR.

All information required for the calculation of the SKR in a CVQKD system is contained in the system's covariance matrix, which is defined as:[35]

$$\Gamma = \begin{bmatrix} (V_A+1)\mathbf{I} & Z\sigma_Z \\ Z\sigma_Z & (1+TV_A+T\xi)\mathbf{I} \end{bmatrix} = \begin{bmatrix} V\mathbf{I} & Z\sigma_Z \\ Z\sigma_Z & W\mathbf{I} \end{bmatrix} \tag{2}$$

where T is the transmittance and ξ is the excess noise (in shot noise units – SNU). The transmittance is the inverse of the overall attenuation experienced by a laser between Alice and Bob due to loss. The excess noise comes from unaccounted noise detected by Bob. $\mathbf{I}$ is the identity matrix and σ_z is the 3rd Pauli matrix, $\begin{bmatrix} 1 & 0 \\ 0 & -1 \end{bmatrix}$. Z is the correlation coefficient, which depends on the specific modulation scheme (refer to ref. [35] for calculation). The parameters in Equation (1) are calculated depending on the coherent state detection measurement.[2,35] Homodyne detection is when only one quadrature is measured at a time. Heterodyne detection occurs when both quadratures are measured simultaneously.

The mutual information is defined as:

$$I_{AB_{\mathrm{hom}}} = \frac{1}{2}\log_2(1+\mathrm{SNR}) \tag{3}$$

for homodyne detection, and

$$I_{AB_{\mathrm{het}}} = \log_2(1+\mathrm{SNR}) \tag{4}$$

for heterodyne detection, where the signal to noise ratio is

$$\mathrm{SNR} = \frac{TV_A}{2+T\xi} \tag{5}$$

Here, the mutual information for heterodyne detection is doubled as both quadratures are measured simultaneously.

The Holevo Bound is defined as ref. [35]:

$$S_{BE} = g\left(\frac{\lambda_1-1}{2}\right) + g\left(\frac{\lambda_2-1}{2}\right) - g\left(\frac{\lambda_3-1}{2}\right) \tag{6}$$

where $g(x) = (x+1)\log_2(x+1) - x\log_2(x)$ and λ_1 and λ_2 are the symplectic eigenvalues of the covariance matrix, Γ. λ_3 is defined as ref. [35]

$$\lambda_{3,\mathrm{hom}} = \sqrt{V\left(V - \frac{Z^2}{W}\right)} \tag{7}$$

for homodyne detection, and

$$\lambda_{3,\mathrm{het}} = V - \frac{Z^2}{W+1} \tag{8}$$

Table 3. Security Parameter Values for Finite Size Limit SKR Calculations.

Security Parameter	Value
d	5
ϵ_s	2×10^{-10}
ϵ	1×10^{-9}
N	1×10^{11}

Table 4. Coefficients of β in the Finite Size Limit.[44]

Coefficient	MLC-MSD	MD
c_1	0.9655	8.250×10^{-2}
c_2	1.507×10^{-4}	0.1834
c_3	-4.696×10^{-2}	0.9821
c_4	-0.2238	-2.815×10^{-5}

The SKR in the finite size limit, assuming a finite number of symbols are sent is defined as ref. [42, 43]:

$$\mathrm{SKR}_{\mathrm{fin}} = f\left[(1-\mathrm{FER})\beta I_{AB} - S_{BE} - \delta n_{\mathrm{privacy}}\right] \tag{9}$$

where f is the laser repetition rate (the amount of symbols transmitted per second), FER is the frame error rate (the rate at which errors arise in one block of the finite key), and $\delta n_{\mathrm{privacy}}$ is the fraction of symbols sent that are excluded for estimating the information gained by Eve that reflects the validity of estimated channel parameters in determining the Holevo Bound.

$\delta n_{\mathrm{privacy}}$ is calculated as ref. [44]:

$$\delta n_{\mathrm{privacy}} = \frac{(d+1)^2}{\sqrt{N}} + \frac{4(d+1)\sqrt{\log_2(\frac{2}{\epsilon_s})}}{\sqrt{N}} + \frac{2\log_2(\frac{2}{\epsilon^2\epsilon_s})}{\sqrt{N}} + \frac{\frac{4\epsilon_s d}{\epsilon\sqrt{N}}}{\sqrt{N}} \tag{10}$$

where d is a discretisation parameter, ϵ_s is a smoothing parameter, ϵ is a security parameter representing the probability that the key is not secret, and N is the total number of symbols sent between Alice and Bob. The details of these different parameters can be found in previous work.[45–48]

Table 3 shows the security parameter values used for finite size limit SKR calculations in ref. [44] for CVQKD with security against collective attacks.[49,50]

Previous experimental CVQKD demonstrations have used laser repetition rates between 10 and 500 MHz.[51–54] Unless otherwise stated, a laser repetition rate of $f = 50$ MHz has been selected for the calculation of finite size limit SKRs, which is near the lower end of the 10–500 MHz range of laser repetition rates used in successfully demonstrated CVQKD, to show modest and more achievable finite size limit SKRs that do not require specialised lasers.

The reconciliation efficiency, β, in the finite size limit depends on the information reconciliation method such as multilevel coding and multistage decoding (MLC-MSD) or multidimensional (MD) reconciliation, which can be used alongside low density parity check (LDPC) codes and depends on the SNR,[40] which is defined as ref. [44]:

$$\mathrm{SNR} = 10\log_{10}\left(\frac{TV_A}{2+T\xi}\right)\ [\mathrm{dB}] \tag{11}$$

The dependency of β on the SNR has been empirically determined as ref. [40, 44]:

$$\beta_{\mathrm{MLC-MSD/MD}} = c_1^{c_2\mathrm{SNR}} - c_3^{c_4\mathrm{SNR}} \tag{12}$$

where the coefficients, c_i, can be found in **Table 4** for MLC-MSD and MD reconciliation.

In addition, the FER depends on the SNR and has been empirically defined as ref.[40, 44]:

$$\mathrm{FER} = \frac{1}{2}\left[1 + m_1\arctan(m_2\mathrm{SNR} + m_3)\right] \tag{13}$$

where $m_1 = 0.8218$, $m_2 = -19.46$, and $m_3 = -298.1$. Note that both β and the FER asymptotically approach 1 as the SNR decreases.[2,44] In addition, Equations (12) and (13) are only valid for values between 0 and 1.[44]

4. Nodes and Links for CVQKD

Figure 3 shows nodes and links that could be used in establishing a CVQKD enhanced global quantum network. The links can be characterised by losses and excess noise that would influence the performance of CVQKD protocols. The nodes would comprise of technologies capable of supporting these links.

For links with multiple sources of loss (A_i), the overall transmittance is defined as:

$$T = \prod_{i=1}^{n}\frac{1}{A_i} \tag{14}$$

where n is the number of sources of loss. Note that A is defined as $\frac{P_T}{P_R}$ where P_T is the transmitted power and P_R is the received power. In general, it is found that for a constant value of noise, larger and more positive SKRs for longer link distances can be achieved in inter-satellite links followed by satellite-to-ground, fiber, and underwater links in order; this can be seen in Appendix A where general trends are also presented.

4.1. Fiber Links

Terrestrial fiber links connect terrestrial nodes such as optical ground stations and are typically embedded in the ground. The transmittance attributed to using a laser in standard fiber is defined as ref. [2, 35]:

$$T_{\mathrm{fiber}} = 10^{-0.02d} \tag{15}$$

and depends on the link distance, d in km, and the fiber attenuation factor. Here, the attenuation factor is 0.02 dBkm^{-1}.[35] It should be noted that investigation of the use of low loss fibers for CVQKD is an ongoing field of development.[55,56] However, for modeling fiber transmissions Equation (15) is used. In fact, the relatively large losses from fiber is a significant reason for moving toward free-space optical communications and QKD.[57]

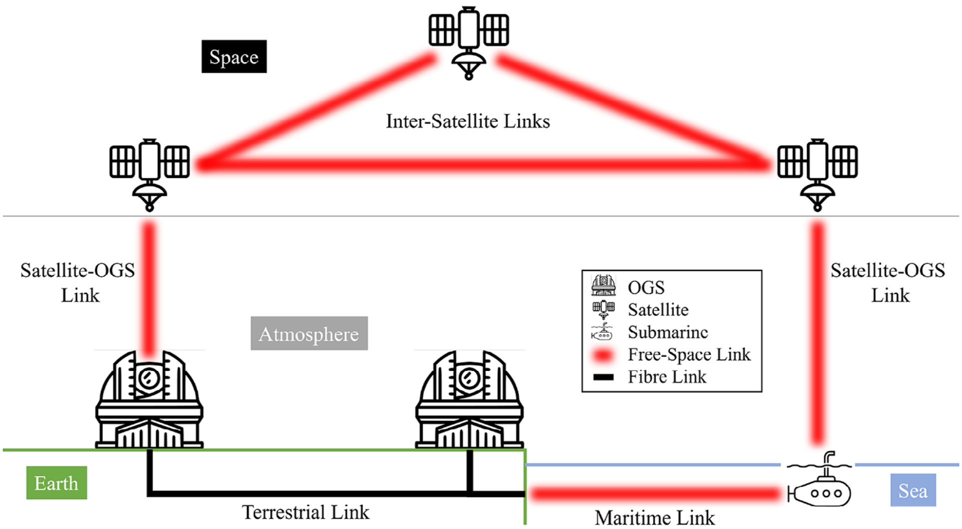

Figure 3. Summary of different nodes and links that could be used in a global quantum network for fiber-based and free-space CVQKD.[25]

4.2. Underwater

Underwater maritime links can be defined as a linear attenuation model, assuming direct line of sight, by calculating the radiative transfer equation following Beer's Law.[58] The transmittance is defined as Refs. [58–60]:

$$T_{\text{underwater}} = \exp\left(-c(\lambda)z\right) \tag{16}$$

where z is the link distance and $c(\lambda)$ is a beam extinction coefficient that is dependent on the wavelength as well as optical absorption and scattering underwater. The beam extinction coefficient is defined as Refs. [58–60]:

$$c(\lambda) = a(\lambda) + b(\lambda) \tag{17}$$

where $a(\lambda)$ is the absorption coefficient and $b(\lambda)$ is the scattering coefficient.

The absorption coefficient is defined as Refs. [61, 62]:

$$a(\lambda) = \left[a_w(\lambda) + 0.06a_c(\lambda)C^{0.65}\right]\left[1 + 0.2\exp(-0.014(\lambda - 440))\right] \tag{18}$$

where a_w is the absorption coefficient of pure water, a_c is the chlorophyll-specific absorption coefficient, and C is the chlorophyll concentration (data are available in Refs. [63, 64]).

The scattering coefficient is defined as:

$$b(\lambda) = 0.3\frac{550}{\lambda}C^{0.62} \tag{19}$$

Although Equations (16)–(19) define the transmittance for all wavelengths, it should be noted that absorption at near-mid infrared wavelengths (1064–1550 nm) is significant. This can be seen from extrapolation of published absorption coefficient data.[63,64] Underwater CVQKD can be operated in the near ultraviolet to visible spectra (400–700 nm). Typical values of $a(\lambda)$ and $b(\lambda)$ are shown in **Table 5** for different water purities at $\lambda = 520$ nm.[62]

Table 5. Absorption and Scattering Coefficients for Water at 520 nm.

Water Type	a (m^{-1})	b (m^{-1})	c (m^{-1})
Pure Sea Water	0.0405	0.0025	0.043
Clear Ocean Water	0.114	0.037	0.151
Coastal Ocean Water	0.179	0.219	0.398
Turbid Harbour Water	0.366	1.824	2.190

4.3. Inter-Satellite Links

Inter-satellite free-space links connect satellites in space. The satellites can be in different orbital altitudes from Earth: [65]

- Low Earth Orbit (LEO): 160-1000 km,
- Geosynchronous equatorial orbit (GEO): 35,786 km, and
- Medium Earth Orbit (MEO): between LEO and GEO.

In space, absorption is negligible and beam wandering can be ignored in the absence of an atmosphere. As a result, losses are attributed solely to diffraction. Assuming perfect alignment between the transmitting and receiving satellites, the transmittance can be modelled as [66]:

$$T_{\text{inter-satellite}} = 1 - \exp\left(-\frac{2r_a^2}{w^2(z)}\right), \tag{20}$$

where z is the link distance, r_a is the radius of the receiver aperture on the receiver satellite. The beam radius, $w(z)$, as a function of the link distance is defined as:

$$w(z) = w_0\left(1 + \left[\frac{\lambda z}{\pi w_0^2}\right]^2\right)^{\frac{1}{2}}, \tag{21}$$

where w_0 is the beam-waist radius and λ is the wavelength.

4.4. Satellite-to-Ground

The main sources of loss in a satellite-to-ground link come from clouds, atmospheric turbulence, and atmospheric aerosols. These correspond to geometric losses from the link distance, scintillation losses from atmospheric turbulence, and scattering losses from atmospheric aerosols.

Atmospheric losses depend on the thickness of the atmosphere and the overall atmospheric mass through which the signal propagates. On average, 95% of the total atmosphere mass is confined to the first 20 km from theground to zenith.[67,68] The overall architecture of a satellite-to-ground link is shown in **Figure 4**. Here, the satellite is assumed to be in LEO and passes over an OGS. The total link distance is calculated as ref. [44]:

$$L_{\mathrm{tot}} = \left(R_{\mathrm{E}} + L_{\mathrm{zen}}\right)^2 + \left(R_{\mathrm{E}} + L_{\mathrm{OGS}}\right)^2 - 2(R_{\mathrm{E}} + L_{\mathrm{zen}})(R_{\mathrm{E}} + L_{\mathrm{OGS}}) \cos(\alpha_1)^{\frac{1}{2}}$$
$$\alpha_1 = \arcsin\left[\cos(\theta) \frac{(R_{\mathrm{E}} + L_{\mathrm{OGS}})}{R_{\mathrm{E}} + L_{\mathrm{zen}}}\right] + (90 - \theta) \tag{22}$$

where $R_{\mathrm{E}} = 6371$ km is the radius of the Earth, L_{OGS} is the altitude of the OGS, L_{zen} is the altitude of the satellite at zenith (90° elevation angle), and $\theta > 0$ is the elevation angle.

The effective atmosphere thickness the signal propagates through is calculated as ref. [44]:

$$L_{\mathrm{atm,eff}} = (R_{\mathrm{E}} + L_{\mathrm{atm}})^2 + (R_{\mathrm{E}} + L_{\mathrm{OGS}})^2 - 2(R_{\mathrm{E}} + L_{\mathrm{atm}})(R_{\mathrm{E}} + L_{\mathrm{OGS}}) \cos(\alpha_2)^{\frac{1}{2}}$$
$$\alpha_2 = \arcsin\left[\cos(\theta) \frac{(R_{\mathrm{E}} + L_{\mathrm{OGS}})}{R_{\mathrm{E}} + L_{\mathrm{atm}}}\right] + (90 - \theta) \tag{23}$$

where $L_{\mathrm{atm}} = 20$ km is the atmosphere thickness from ground to zenith containing 95% of the total atmospheric mass.

A satellite-to-ground link is characterized differently depending on the direction of transmission. It can either be a downlink (satellite-to-ground) or uplink (ground-to-satellite). This is because the link is not uniform and contains both the atmosphere and space environments. Uplinks are known to be more difficult as the signal is degraded by the atmosphere first, causing significant beam wandering and increase in scintillation by the time it reaches the satellite resulting in larger losses.[69–73]

Table 6 summarises 'good' and 'bad' atmospheric weather conditions used for the calculation of SKRs.[44]

4.4.1. Satellite Downlink

Geometric loss is defined as ref. [69]:

$$A_{\mathrm{geo}} = 10\log_{10}\left(\frac{L_{\mathrm{tot}}^2 \lambda^2}{D_{\mathrm{t}}^2 D_{\mathrm{r}}^2} \frac{1}{T_{\mathrm{t}}(1 - L_{\mathrm{p}}) T_{\mathrm{r}}}\right) [\mathrm{dB}] \tag{24}$$

where λ is the wavelength, D_{t} is the transmitter aperture diameter, D_{r} is the receiver aperture diameter, T_{t} is the transmitter optics efficiency, T_{r} is the receiver optics efficiency, and L_{p} is the pointing loss that can be attributed to the inefficiency of an acquisition, pointing, tracking (APT) system of the OGS, as well as beam wandering. Equation (24) assumes that the receiver is in the far field ($L_{\mathrm{tot}} > \frac{D_{\mathrm{t}} D_{\mathrm{r}}}{\lambda}$), the transmitter is diffraction limited, and there is no attenuation from the atmosphere, enabling the addition of other atmospheric losses (scattering and scintillation losses).

Atmospheric aerosols give rise to scattering losses through Rayleigh scattering, Mie scattering, and geometrical scattering.[74] At a wavelength of 1550 nm, the effects of Rayleigh scattering are negligible and the effects of geometrical scattering, from rain, snow, and hail, are ignored as satellite-to-ground CVQKD, in general, is not possible during these weather conditions, as they could cause damage to the telescope in an OGS.[44]

Mie scattering is defined through the Kruse and Kim model as ref. [75]:

$$A_{\mathrm{scat}} = 10\log_{10}(e)\left(\frac{3.912}{V}\right)\left(\frac{\lambda}{550}\right)^{-p} [\mathrm{dB/km}],$$
$$p = \begin{cases} 1.6 & V \geq 50\ \mathrm{km} \\ 1.3 & 6\ \mathrm{km} \leq V < 50\ \mathrm{km} \\ 0.16V + 0.34 & 1\ \mathrm{km} \leq V < 6\ \mathrm{km} \\ V - 0.5 & 0.5\ \mathrm{km} \leq V < 1\ \mathrm{km} \\ 0 & V < 0.5\ \mathrm{km} \end{cases} \tag{25}$$

Scintillation loss from atmospheric turbulence is defined as ref. [76]:

$$A_{\mathrm{sci}} = 4.343\left(\mathrm{erf}^{-1}(2p_{\mathrm{thr}} - 1)\left[2\ln(\sigma_I^2 + 1)\right]^{\frac{1}{2}} - \frac{1}{2}\ln(\sigma_I^2 + 1)\right) \ [\mathrm{dB}] \tag{26}$$

where σ_I is the scintillation index and p_{thr} is the probability that the received power is below the minimum required to register a signal (equivalent to the fraction of link outage time).

The scintillation index, assuming a spherical wave, is defined as:

$$\sigma_{\mathrm{I}}^2(D_{\mathrm{r}}) = \exp\left\{\frac{0.20\sigma_R^2}{[1 + 0.18d^2 + 0.20(\sigma_R^2)^{\frac{6}{5}}]^{\frac{7}{6}}} + \frac{0.21\sigma_R^2[1 + 0.24(\sigma_R^2)^{\frac{6}{5}}]^{-\frac{5}{6}}}{1 + 0.90d^2 + 0.21d^2(\sigma_R^2)^{\frac{6}{5}}}\right\} - 1 \tag{27}$$

where σ_R is the Rytov variance and $d = D_{\mathrm{r}}\left(\frac{\pi}{2\lambda_{\mathrm{atm,eff}}}\right)^2$.

The Rytov variance is defined as:

$$\sigma_R^2 = 2.25k^{\frac{7}{6}} \int_0^{L_{\mathrm{atm,eff}}} C_n^2(z)(L_{\mathrm{atm,eff}} - z)^{\frac{5}{6}}\, dz \tag{28}$$

where $k = \frac{2\pi}{\lambda}$ is the wave number and C_n^2 is the refractive index structure parameter describing the intensity of turbulence in the atmosphere.

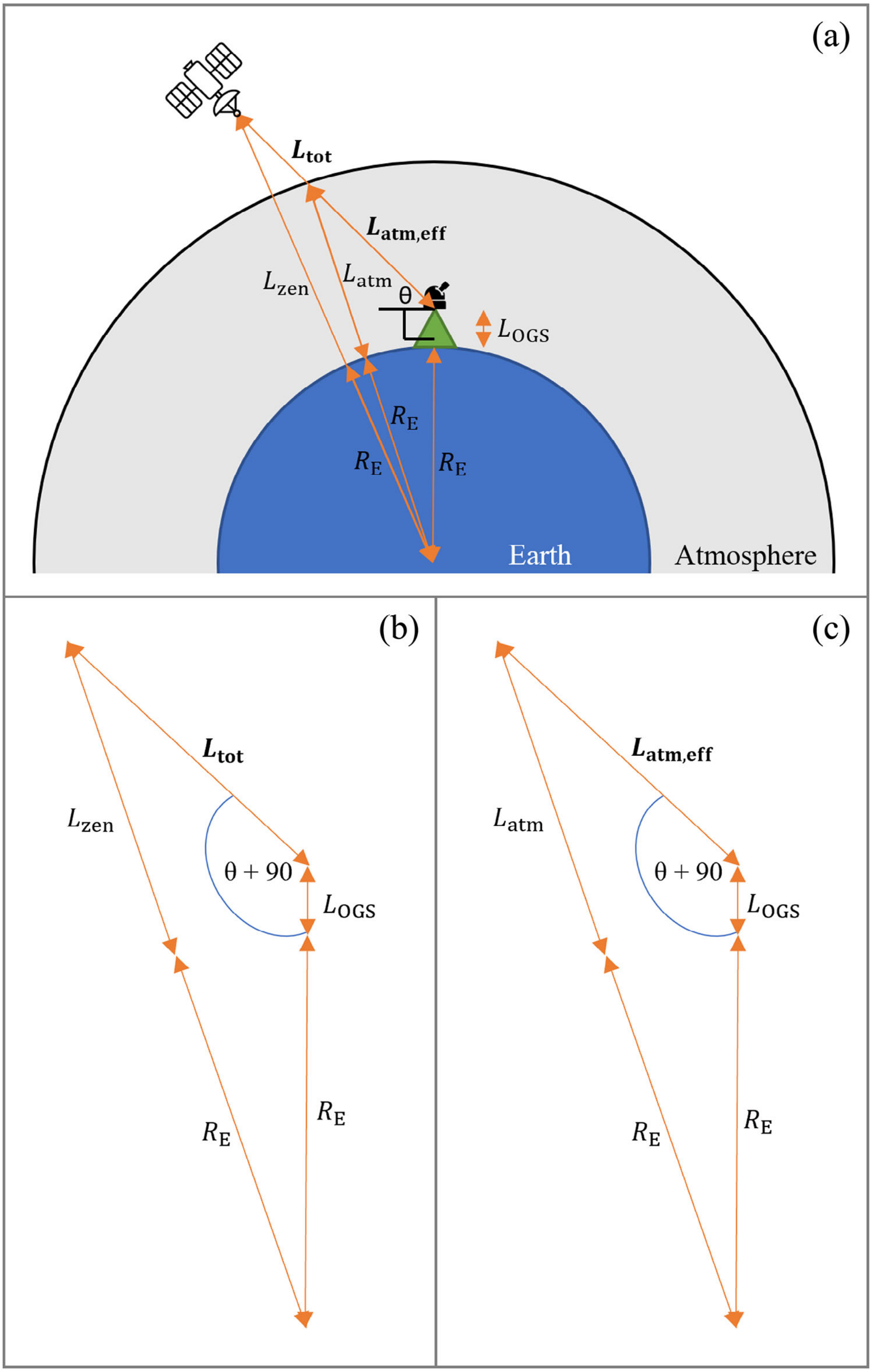

Figure 4. The satellite-to-ground channel model is shown in (a). Diagrams (b) and (c) shows the trigonometric determination of the total link distance (L_{tot}) and effective atmosphere thickness ($L_{atm,eff}$), respectively. L_{atm}: atmosphere thickness at zenith (20 km), L_{zen}: satellite altitude at zenith, L_{OGS}: OGS altitude, θ: elevation angle, R_E: mean radius of the Earth (6371 km).[44]

Table 6. Atmospheric Parameters in Satellite-to-Ground Links.

Parameter	Good	Bad
Atmospheric Visibility, V	200 km	20 km
Refractive Index Structure Parameter, C_n^2	10^{-16} m$^{-2/3}$	10^{-12} m$^{-2/3}$

C_n^2 can be empirically defined as ref. [77]:

$$C_n^2(h) = 0.00594\left(\frac{w}{27}\right)^2 (h \times 10^{-5})^{10} \exp\left(-\frac{h}{1000}\right) + 2.7 \times 10^{-16} \exp\left(-\frac{h}{1500}\right) + A \exp\left(-\frac{h}{100}\right) \tag{29}$$

for altitudes between 3 and 24 km (within the 20 km atmospheric thickness,[67,68]) where w is the wind speed, h is the altitude, and A is the is the nominal value of C_n^2 at $h = 0$. Alternatively, C_n^2 can be defined qualitatively where $C_n^2 = 10^{-16}$ describes a low turbulent atmosphere, $C_n^2 = 10^{-14}$ a medium turbulent atmosphere, and $C_n^2 = 10^{-13}$ a high turbulent atmosphere.[78]

4.4.2. Satellite Uplink

In an uplink, losses are more prominent as the beam is exposed to the atmosphere first.[69–71] This causes significant beam wandering and scintillation.[79] The uplink model can use most of the sources of loss found in a downlink with a few exceptions:

- $L_{\text{p,uplink}} > L_{\text{p,downlink}}$ to account for greater beam wandering,
- $\sigma^2_{I,\text{uplink}} > \sigma^2_{I,\text{downlink}}$ to account for larger scintillation loss.

The beam wandering arises from the difference in refractive index between the atmosphere and space. By propagating through the atmosphere first, the laser is deflected from its original path earlier and therefore will have greater deviation from the intended path to the satellite by the time it reaches the satellite altitude. This is represented as an increase in the pointing loss (L_P) in the satellite-to-ground model. However, this could be mitigated by APT systems and optics, which are more easily implemented in an OGS than a satellite.[50] The same pointing loss, $L_P = 0.1$ is therefore used for both uplink and downlink SKR calculations.

In contrast, for a given turbulence strength, quantified by the refractive index structure parameter (C_n^2), uplinks have greater scintillation indices (σ_I) compared to downlinks.[72,73] The difference between the uplink and downlink scintillation index increases as a function of the elevation angle. For a wavelength of 1550 nm and turbulence of $C_n^2 = 10^{-14}$ m$^{-2/3}$ (medium turbulence), the difference in scintillation index increases asymptotically to $\sigma_{I,\text{uplink}} - \sigma_{I,\text{downlink}} = 0.2$.[73] For a weaker turbulence ($C_n^2 = 10^{-16}$ m$^{-2/3}$), it is expected that the difference between uplink and downlink scintillation indices would decrease. To prevent an underestimation of scintillation indices in uplinks, the following relation between uplink and downlink scintillation indices is used for all elevation angles:

$$\sigma_{I,\text{uplink}} = \sigma_{I,\text{downlink}} + 0.2 \tag{30}$$

Table 7. Sources of Excess Noise.

Link Type	Excess Noise Source
Fiber	Vibrations, heat
Underwater	Precipitates, small organisms, heat currents
Inter-satellite	Radiation
Satellite-to-ground	Atmospheric aerosols, atmospheric turbulence

4.5. Sources of Noise

In physical application, the excess noise will vary depending on the link. In an ideal system where coherent states are transmitted, received, and measured with a variance of 1 SNU, the excess noise represents unaccounted noise above this shot noise limit. For example, given the electronic noise is trusted, the excess noise in a transmitted shot noise limited coherent state with a measured variance of 1.2 SNU is 0.2 SNU. **Table 7** shows different sources of excess noise that may be found in the link types modeled. Excess noise stems from coherent states that have undergone decoherence as well as measured photons, which have not been taken into account.

5. Developing a Dynamic Global CVQKD Network

A general network can be represented as a graph. Secret key distribution through a CVQKD network can be modeled as a graph problem where the secret key traverses through the graph to be shared between different nodes. The concept of the link capacity, which represents the maximum size of the secret key that can be transmitted in a link, is presented and can be used as a guide to determine optimum paths through a CVQKD network.

5.1. Link Capacity

The SKR is a valuable metric for showing the performance of a CVQKD protocol in a link. However, it does not include a key parameter; the time taken for transmitting coherent states and generating a secret key between nodes. The overall capacity of a link can be determined. The link capacity represents the maximum size of the secret key that can be transmitted in a link (note that the SKR is a lower bound and so the link capacity also becomes a lower bound).

The link capacity can be presented as:

$$C = \text{SKR} \times t \tag{31}$$

where SKR is the finite size limit SKR and t is the period of time that the link can be used (positive SKR) to transmit the secret key. It is important to note that t is not necessarily an arbitrary period of time. In satellite-to-ground links, it represents the usable period during a pass of a satellite over an OGS. In this case, there is a different SKR for each time increment as the satellite track varies in elevation angle and consequently varies in link distance. In contrast, t has a single value in the case of fiber links as both nodes are stationary and there are no geometric dependencies other than a constant length.

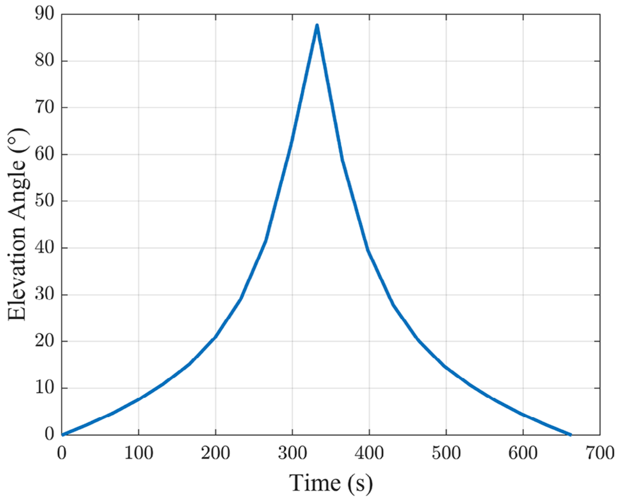

Figure 5. Elevation angles for an ISS pass over Mt. John Observatory on 9th August 2022. The pass had a maximum elevation angle of 87.6°.

In the case of secret key distribution through a CVQKD network, the link capacity acts as a guide to determine the optimum path, through nodes and links, through which a secret key can be distributed. For a practical multi-node distribution, the following link capacity conditions must be met:

- The link capacity of subsequent links must be greater than the link capacity of the first link. This ensures that there are no links acting as a bottleneck during distribution, and
- All link capacities in a series of nodes and links must be greater than the size of the secret key being transmitted. This ensures that there is no information loss of the secret key during distribution.

To show how the link capacity can be used, satellite-to-ground and inter-satellite links have been simulated.

5.1.1. Satellite-to-Ground Link Simulation

Simple Downlink: Calculation of the link capacity has been performed between the University of Canterbury's Mt John Observatory (MJO) in New Zealand (Latitude = −43.9853°, Longitude = 170.4641°, Altitude = 1.029 km) and the International Space Station (ISS) for a downlink scenario.[44] Here, it was assumed that there is a CVQKD receiver at MJO and a CVQKD transmitter on the ISS. The ISS pass details were sourced from Gpredict[80] for the 9th August 2022 and had a duration of 663 s with a maximum elevation angle of 87.6° (shown in **Figure 5**).

The calculation of the link capacity[44] is modified using a recent formulation of GM-CVQKD[35] for the calculation of the finite size limit SKR. In addition, an OGS altitude of L_{OGS} = 1.029 km, good atmospheric conditions ($C_n^2 = 10^{-16}\text{m}^{-2/3}$, V = 200 km), and ISS altitude of L_{zen} = 408 km are used. **Figure 6** shows the finite size limit SKRs as a function of the elevation angle.

Multiplying the calculated SKR by the time that the ISS is at a discrete elevation angle (Equation (31)) gives the maximum number of bits that can be transmitted during the downlink with

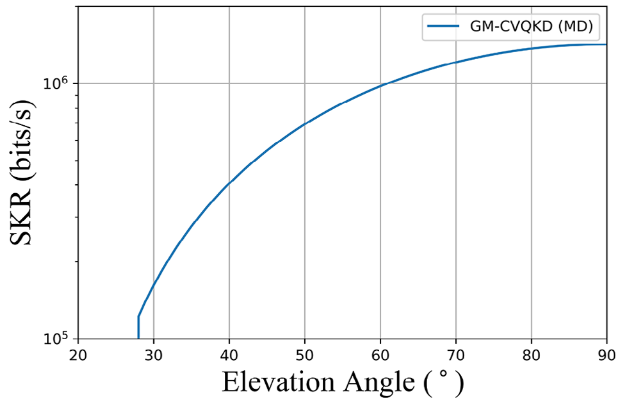

Figure 6. Downlink finite size limit SKRs for GM-CVQKD using MD reconciliation as a function of the elevation angle. V_A = 5 SNU, β = 0.9, ξ = 0.03 SNU, D_R = 1m, D_T = 0.3m, L_{zen} = 408 km, L_{OGS} = 1.029 km.

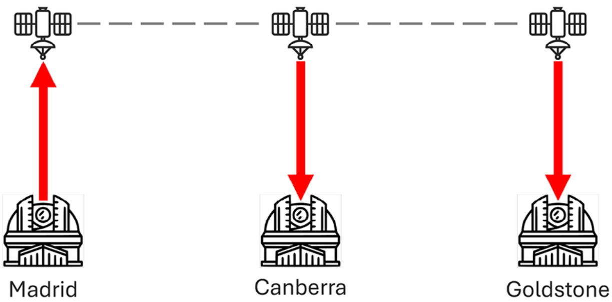

Figure 7. Schematic of the uplink and downlinks scenario for the ISS passing over the three DSN ground station sites.

GM-CVQKD with MD reconciliation. The elevation angle has been discretised with a resolution of 1° in Figure 5 to determine the temporal position of the ISS. In this case, the link capacity is 155 Mbit if transmission were to occur during the pass when the elevation angle produces positive SKRs.

Uplink and Downlink through the Deep Space Network: The importance of the link capacity is better demonstrated when there are multiple nodes and links used to distribute a secret key. For this case, a series of uplinks and downlinks are simulated using the locations of the Deep Space Network (DSN) with ground stations in Madrid (Latitude = 40.4298°, Longitude = −4.2489°), Goldstone (Latitude = 35.2828°, Longitude = −116.7840°), and Canberra (Latitude = −35.4025°, Longitude = 148.9829°),[81] and the ISS (orbit altitude of L_{zen} = 408 km).

A scenario was modelled using CVQKD where the distribution of the secret key with an uplink from Madrid to the ISS, downlink from the ISS to Canberra, and downlink from the ISS to Goldstone (**Figure 7**), where each transmission occurs when the ISS passes over the field of view of each ground station. The passes of the ISS over the three ground stations were again estimated with Gpredict,[80] and are presented in **Figure 8**.

The corresponding uplink and downlink finite size limit SKRs used to calculate the link capacities are the SKR profiles shown in **Figure 9**. Similar to the simple downlink simulation, the SKR at each elevation angle was multiplied by the duration that the ISS spends at that elevation angle, where the elevation angle has been discretised into 1° increments.

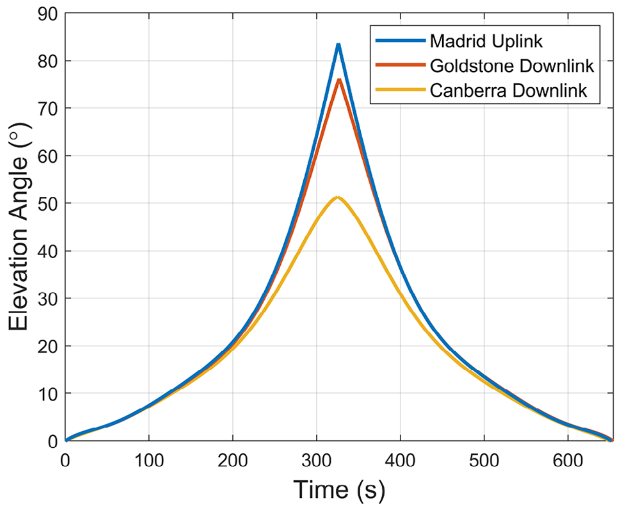

Figure 8. Elevation angles of ISS passes over Madrid, Goldstone, and Canberra DSN ground stations.

Table 8 shows the maximum uplink and downlink link capacities. It can be seen that although the Madrid pass reaches the highest elevation angle of all the passes (Figure 8), it does not yield the largest link capacity. This is because the uplink SKR profile (Figure 9a) only produces positive SKRs above an elevation angle of approximately 73°, and the ISS pass spends less time at larger elevation angles. Similarly, the Canberra pass does not yield the smallest link capacity because the downlink SKR profile (Figure 9b) has a smaller minimum elevation angle (approximately 29°), and the ISS pass spends more time at smaller elevation angles.

Given that the secret key size (SK) transmitted is less than or equal to 3.71 MBit, the scenario is feasible according to the link capacity criteria as

1. Subsequent links have a greater link capacity than the first link:
   $C_{\text{Canberra,downlink}}, C_{\text{Goldstone,downlink}} > C_{\text{Madrid,uplink}}$, and
2. All link capacities are greater than the size of the secret key being transmitted:
   $C_{\text{Madrid,uplink}}, C_{\text{Canberra,downlink}}, C_{\text{Goldstone,downlink}} > \text{SK}$.

Table 8. Link Capacity for each Uplink and Downlink.

	Madrid Uplink	Canberra Downlink	Goldstone Downlink
Link Capacity (MBit)	3.71	61.53	121.25

5.1.2. Inter-Satellite Link Simulation

A satellite pass over an OGS with a large field of view (and therefore a large range of available elevation angles) to support large SKRs and link capacities is infrequent in most locations. A promising solution is the use of inter-satellite links. In this case, a satellite with the secret key from an OGS uplink can pass the secret key via a chain of satellites until a satellite within an acceptable field of view over the receiving ground station is reached.

The minimum number of inter-satellite links between Madrid and Goldstone, and Madrid and Canberra can be found by assuming the link capacity values in Table 8. This scenario is presented in **Figure 10** with the calculated distances and central angles shown in **Table 9**. The chain of satellites were assumed to be at the same altitude as the ISS i.e. $h_s = 408$ km.

The inter-satellite link finite size limit SKR profile in **Figure 11** is used to calculate the link capacity. The SKR at 1000 km is approximately 3000 Mbits^{-1} for GM-CVQKD with MD reconciliation. Each link in the inter-satellite chain only needs to be greater than the Madrid uplink link capacity, which is 3.71 MBit. This requires a transmission time greater than 1.2 ms and results in a central angle between adjacent satellites of $\phi = 8.46°$. This would correspond to 9–10 links and 10–11 satellites in the Madrid to Goldstone inter-satellite chain, and 18–19 links and 19–20 satellites in the Madrid to Canberra inter-satellite chain.

An inter-satellite link distance of 1000 km between adjacent satellites at an altitude of 408 km has the entire laser link at an altitude above the atmosphere (which has a thickness of 20 km.[67,68]) For longer distances, made possible by larger apertures, it is important that the laser does not propagate through the atmosphere to avoid atmospheric losses. This is ensured by optimising values for ϕ and L_n so that the laser is above 20 km.

5.2. Global CVQKD Network: A Dynamic Graph Problem

The different types of links that could be used for establishing a global CVQKD network are classified here and shown in **Table 10**.

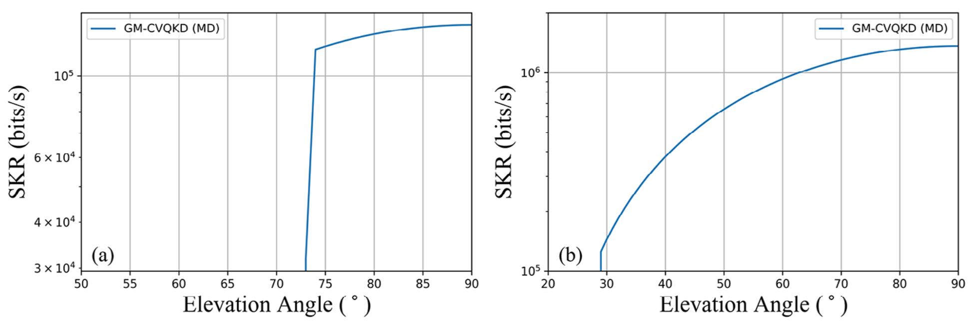

Figure 9. a) Uplink and b) downlink finite size limit SKRs for GM-CVQKD using MD reconciliation as a function of elevation angle. Using MLC-MSD reconciliation did not produce positive SKRs. $D_R = 0.3$ m, $D_T = 1$ m, $L_{zen} = 408$ km.

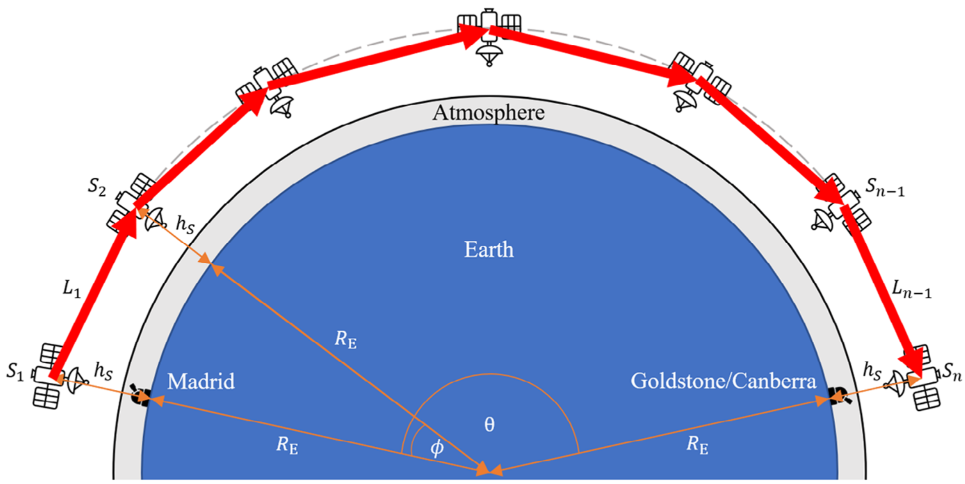

Figure 10. A schematic of secret key distribution between Madrid and Goldstone/Canberra using inter-satellite links. S : Satellite, L: Inter-satellite link, n: Number of satellites in the chain of inter-satellite links, R_E: Earth radius, h_S: Satellite orbit altitude, θ: Central angle between the two ground stations (Madrid and Goldstone/Canberra), ϕ: Central angle between two satellites with an inter-satellite link.

Table 9. Distances and Central Angles between Madrid and Goldstone/Canberra.

Link	Ground Distance (km)	Distance @ 408 km Altitude (km)	Central Angle (°)
Madrid to Goldstone	9,200	9,789	83
Madrid to Canberra	17,600	18,727	158

The geometry of the link is dependent on whether a node is stationary (fixed location) or moving (varying location). Stationary-to-stationary node links are the simplest but are confined to relatively small distances due to the relatively high attenuation in fiber links. Stationary-to-moving node links require an APT system that enables the capture and tracking of the moving node. Moving-to-moving node links requires APT systems with high resolution and fast tracking as there is relative motion between the nodes.

As the link capacity is time dependent, the three types (stationary–stationary, stationary–moving, moving–moving) are classified here into static or dynamic links (Table 10). A static link is where the link capacity is only dependent on the transmission time. This occurs when the link is spatially fixed and contains no moving transmitters and receivers. Dynamic links occur when the link capacity is dependent on both the transmission time and the link geometry between the transmitter and receiver as the link distance between them can vary.

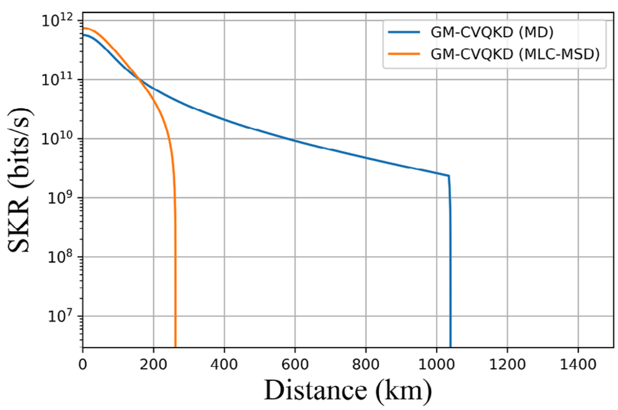

Figure 11. Inter-satellite based finite size limit SKRs for GM-CVQKD using MLC-MSD and MD reconciliation. $r_a = w_0 = 0.2$ m.

Table 10. Classification of Different Links.

Link	Geometry	Static/ Dynamic	Uniform/ Non-Uniform
Fiber	Stationary-Stationary	Static	Uniform
Satellite-to-Ground	Stationary-Moving	Dynamic	Non-Uniform
Submarine-to-Ground	Stationary-Moving	Dynamic	Uniform
Satellite-to-Submarine	Moving-Moving	Dynamic	Non-Uniform
Inter-Satellite	Moving-Moving	Dynamic/ Static	Uniform
Inter-Submarine	Moving-Moving	Dynamic	Uniform

Uniform links are defined here as when the channel between the transmitter and receiver can be thought of as isotropic. For example, inter-satellite links ideally have the vacuum of space between the transmitter and receiver,[66] and the channel in inter-submarine (underwater) links can be modelled as water with an average chlorophyll concentration.[61,62] In contrast, non-uniform links have a non-isotropic channel where the link capacity is direction-dependent. This is appropriate for satellite-to-ground links where the SKR and link capacity differ between uplinks and downlinks because the channel contains both the atmosphere and the vacuum of space (Figure 3). In addition, the channel changes during a satellite pass since the total link distance and effective atmosphere thickness changes.

It should be noted that if a constellation of satellites were developed where the relative positions between each satellite were fixed through active propulsion, then inter-satellite links

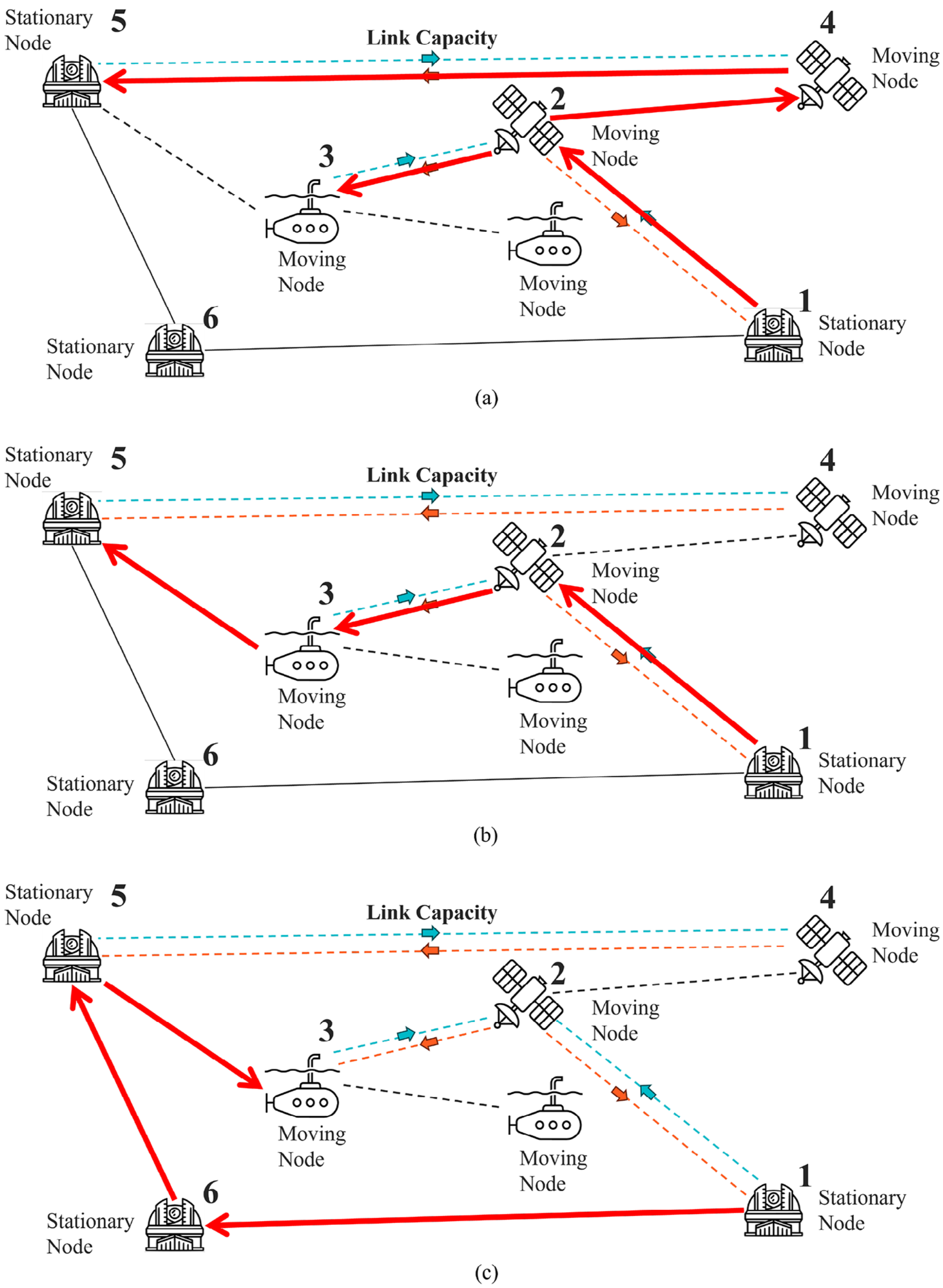

Figure 12. Possible pathways to distribute a secret key between an OGS (1), submarine (3), and another OGS (5).

are static (as modelled in Section 5.1.2). This is because the relative distance between each satellite remains fixed. In addition, submarine-to-ground links would require an OGS to be near the coast with direct access to the sea to form a uniform link with a submarine where the only environment is sea-water.

The different nodes and links can be represented graphically as shown in **Figure 12**, where the nodes comprise the different CVQKD transmitters and receivers, and the edges comprise the different link types. The weights represent the link capacity. Figure 12 also shows a hypothetical scenario where a secret key is to be distributed between an OGS (1), a submarine (3), and another OGS (5). In this case, there can be three pathways as shown in Figure 12.

The availability and use of different links depends on factors such as the weather, and spatiotemporal availability of nodes,.[82] For a graph, the link capacity can be used as the "cost" to traverse through different links throughout the network. Shortest path algorithms could be employed, such as Dijkstra's algorithm,[83] to find the optimum path to distribute the secret key to the desired nodes. Here, the optimum path would be the links with the largest link capacities while satisfying the link capacity conditions for multi-node transmissions.

In a general QKD network architecture (Figure 2), the network manager would track the position of nodes and monitor the dynamic link capacities in real-time. In addition, the network manager would determine and monitor the optimum path between nodes for CVQKD based on the link capacities at any given time should a request arise for secret key distribution.

6. Discussion

The SKR of different CVQKD in different link types have been analysed in the asymptotic and finite size limit. In the finite size limit, GM-CVQKD with MD reconciliation outperforms all other protocols. So far, CVQKD has been implemented in fiber and short-distance horizontal free-space. However, a full-stack implementation in all link types with post-processing is yet to be realized in addition to physical implementation in other link types such as satellite-to-ground, inter-satellite, and underwater links.

In high-speed CVQKD deployments, particularly over fiber and free-space links, chromatic dispersion and related spectral broadening effects can distort the temporal mode structure of the transmitted signal, leading to degraded quadrature measurements and reduced secret key rates. Recent work has demonstrated that digital signal processing (DSP) techniques can be used to characterize and mitigate these impairments by projecting the received signal onto a reference temporal mode and evaluating a mode-matching coefficient.[84] This coefficient quantifies the overlap between the distorted and ideal modes, enabling a qualitative assessment of performance under channel dispersion. Additionally, in satellite-based CVQKD, Doppler shifts from orbital motion introduce frequency offsets and timing mismatches that further distort the received signal. These effects are particularly significant in low Earth orbit systems, where relative velocities exceed 7 $\mathrm{kms^{-1}}$. Experiments such as those conducted by the Micius satellite[85] underscore the importance of frequency and phase tracking to maintain quantum coherence in the presence of Doppler-induced drift. While this study focuses on large-scale network modeling, future integration of DSP-based dispersion and Doppler compensation will be critical to enabling robust, high-speed CVQKD across heterogeneous link types.

The simulated inter-satellite scenario is idealized (Section 5.1.2). It assumes that adjacent satellites are within line-of-sight of each other with adequate APT systems for alignment. In addition, it assumes instantaneous/negligible processing time of the secret key. In reality, this is not the case and processing will cause a delay in transmitting a secret key between satellites. Sources of delay may include the time taken to align satellite transmitter and receiver apertures, decode the received secret key and re-transmit to another satellite (in the case of a trusted satellite), relay the secret key through quantum repeaters. The satellites in the chain are also assumed to be trusted. This gives assumed security within each satellite node where Eve cannot access it. However, if any of the satellite are not trusted, quantum repeaters[86,87] would be required to maintain security. The scenario assumes well-positioned and consistently spaced satellites within the chain. In reality, the satellites orbit with different trajectories and a smaller number of satellites may be required when transmitting the secret key as the satellites move. The satellite trajectories are predictable and the route could be optimized.

As developments in CVQKD progress, a global quantum network secured by CVQKD can be modelled virtually. Real-time locations of nodes and possible links between nodes can be modelled and implemented in such a virtual network. The spatiotemporal feasibility of CVQKD in different link types would depend on the link capacity, which is dependent on the dynamic SKR for links involving moving nodes, such as in the simulations performed for satellite-to-ground and inter-satellite links. Real-time weather and environmental conditions could also be included to simulate potential adversities that could be present in the different links. In addition, a governing network architecture could be implemented, simulating a CVQKD secured global quantum network. The network manager would monitor parameters related to CVQKD and the weather/environment across the network. In particular, the link capacity to determine the optimum path when nodes and users request a secret key. The virtual network would act as a foundation for physically deploying CVQKD in a global quantum network when the necessary developments are made such as experimentally validated CVQKD in different link types, integration of different links, and controllability of links and nodes.

In developing a global quantum network secured with general QKD, it is important to use the already existing resources such as current national networks around the world. Since these networks are predominantly DVQKD-based, CVQKD would be an addition to the network; creating a hybrid global quantum network, which uses both CVQKD and DVQKD. However, it is of upmost importance that different links in a global quantum network will require different laser technology and detection methods to extract the maximum SKR. An example of this is the different transmission windows found in the atmosphere[88] are different to underwater[63,64] leading to different wavelengths being used for the links, and thus the proper wavelength laser and a high efficiency detector at the appropriate wavelength, to optimize the SKR. In addition, appropriate transmitter and receiver technologies would be required to further maximize the SKR. For example, turbulent atmospheric channels would require adaptive optics to correct wavefront aberrations,[89] and inter-satellite links would require a feedback mechanism to ensure line of sight and maximum power on the receiver.[90] These different design solutions would make a more diverse network hosting a variety of transceiver technologies. The network would still require a governing network architecture. Therefore, this architecture would require compatibility with both CVQKD, DVQKD, and all other technologies found in the different links and nodes in existing QKD networks. In addition, future implementations e.g., for CVQKD, would also need to be compatible.

The application of shortest path algorithms for finding the optimum path for secret key distribution requires frequent updates.[91] Since there are moving nodes and dynamic links, in addition to varying environmental conditions, the optimum path would vary with time. This would depend on a range of variables such as the real-time positions of nodes, link distances, and the losses involved in the links, which are environment-dependent. The positions of nodes and therefore links must be tracked in combination with environmental parameters such as the weather (e.g., turbulence) and chlorophyll concentrations to determine real-time link capacities across the network. This could be achieved by keeping track of satellite TLEs (two line elements), submarine positions, and the chlorophyll concentration of the waters they are in when revealed, the locations of OGSs in use, and therefore the dynamic link capacities across the network.

The distribution of secret keys through different paths across a network (Figure 12) assumes a trusted node framework (trusted relay implementation) in which the secret key can simply be received and transmitted through different nodes as they are assumed to be resilient to eavesdroppers. However, there is the case where certain nodes cannot be trusted, and therefore passing a secret key through them poses a security risk. The underlying assumption in QKD is that any unaccounted for noise/loss detected above an upper bound threshold can be attributed to the presence of an eavesdropper.[92–94] In the case of remote nodes such as satellites, increases in noise can be detected but its source cannot always be determined. For example, a spike in noise can be attributed to system malfunction (e.g., overheating of detectors) or an actual eavesdropper. To combat this problem, quantum repeaters that are compatible with CVQKD must be used.[86,87] In this case, a secret key passing through a node is not measured but simply relayed onto the next node. Since the secret key is not measured at a node, then any technical problems leading to noise variations in a fully functioning node with a quantum repeater can be blamed solely on an eavesdropper tampering with the node. Although quantum repeaters are suitable for this endeavor, they are currently in development[95] and have yet to be used for satellite applications.

A method for secret key distribution is to build up storage of secret keys over time at certain locations (nodes) where users can then request the use of secret keys.[4] This can be achieved with satellite-to-ground CVQKD where secret keys are generated and stored during good weather conditions. A network of different nodes and links could improve upon this by helping store secret keys by providing alternative paths when certain links are not available (from bad channel parameters e.g., bad weather conditions) through spatial diversity. The use of shortest path algorithms in combination with link capacities could provide optimum paths for secret key distribution in this endeavor.

The links established using OGS, satellite, and submarine nodes were used in the context of a CVQKD network. The addition of high-altitude platforms such as (space) planes, unmanned aerial vehicles, and drones adds another dimension for faster real-time CVQKD in localized areas.[23,96] The controllability of these platforms could allow for more targeted CVQKD avoiding reliance on the trajectories of nodes such as satellites, providing more spatial diversity and interconnectedness. In addition, they have the potential to operate in all weather-conditions and can connect ground and satellite platforms together.[23] Moreover, the development of transportable OGSs (TOGSs)[97] provides further spatial diversity on the ground. This could give rise to more dynamic links and easier access to secret keys.

7. Conclusion

A study of the structure of different QKD networks around the world showed different numbers of architectural layers in each network. The different layers were fit into a general three-layer QKD network architecture, which consists of an application layer, control and management layer, and infrastructure layer representing how the different networks could be combined into an overarching global QKD network. The existing QKD network layers would have to be adapted to fit within the three-layer QKD network architecture. The use of an SDN controller would help ease the integration of new nodes as well as integration into existing telecommunication networks.

In general, a larger and more positive SKR for longer link distances can be achieved in inter-satellite links followed by satellite-to-ground, fiber, and underwater links in order. This is based on the analysis of different transmittance models inherent to each link in combination with constant values of modulation variance, reconciliation efficiency, and excess noise. Since the performance of CVQKD differs in each link type, spatiotemporal diversity of nodes is beneficial to combat situations where dynamic links become unfavorable to distribute a secret key.

Different links that can be used in a global QKD network were classified and such a network was presented as a graph problem. The link capacity, which considers a dynamic SKR based on a dynamic link (consisting of moving nodes) and its dynamic parameters, was developed to calculate the maximum lower bound of information that can be stored in the secret key in a link for CVQKD. This can be used as a routing metric to determine the feasibility of secret key distribution between different nodes across a network. In addition, the link capacity, in combination with search algorithms, can help determine the optimum path through a CVQKD network that hosts a plethora of dynamic and non-dynamic links.

Appendix A: SKR as a Function of Distance

Analysis of the different parameters that affect different links show that there are multiple ways to increase the SKR. The parameters inherent to each link are based on the SKR calculation in Section 3 and the transmittance/loss equations found in Section 4.

In general, the following results in more positive and larger SKRs:

- Larger transmittance by mitigating losses,
- Smaller excess noise from better characterization of sources of noise,
- Optimized modulation variance from more accurate characterization of links and the covariance matrix,
- Higher correlation coefficient from more accurate estimation of modulation variance,
- Higher reconciliation efficiency from high performance information reconciliation codes,
- Higher repetition rate from laser systems, and
- Smaller $\delta n_{\text{privacy}}$ from more accurate estimates of the Holevo bound and more symbols sent.

Fiber Links: The main parameter in fiber links is the attenuation factor. Decreasing this leads to larger transmittances and therefore more positive and higher SKRs.

Satellite-to-Ground/Submarine Links: Favorable atmospheric conditions and optimization of a CVQKD system lead to more positive and larger SKRs. In this case:

- Increasing the transmitter and receiver aperture diameter, as well as the transmitter and receiver optics efficiencies increases the transmittance and therefore the overall achievable link distance.
- Decreasing the pointing loss increases the maximum link distance and therefore satellite orbit altitude. This requires more accurate APT systems.

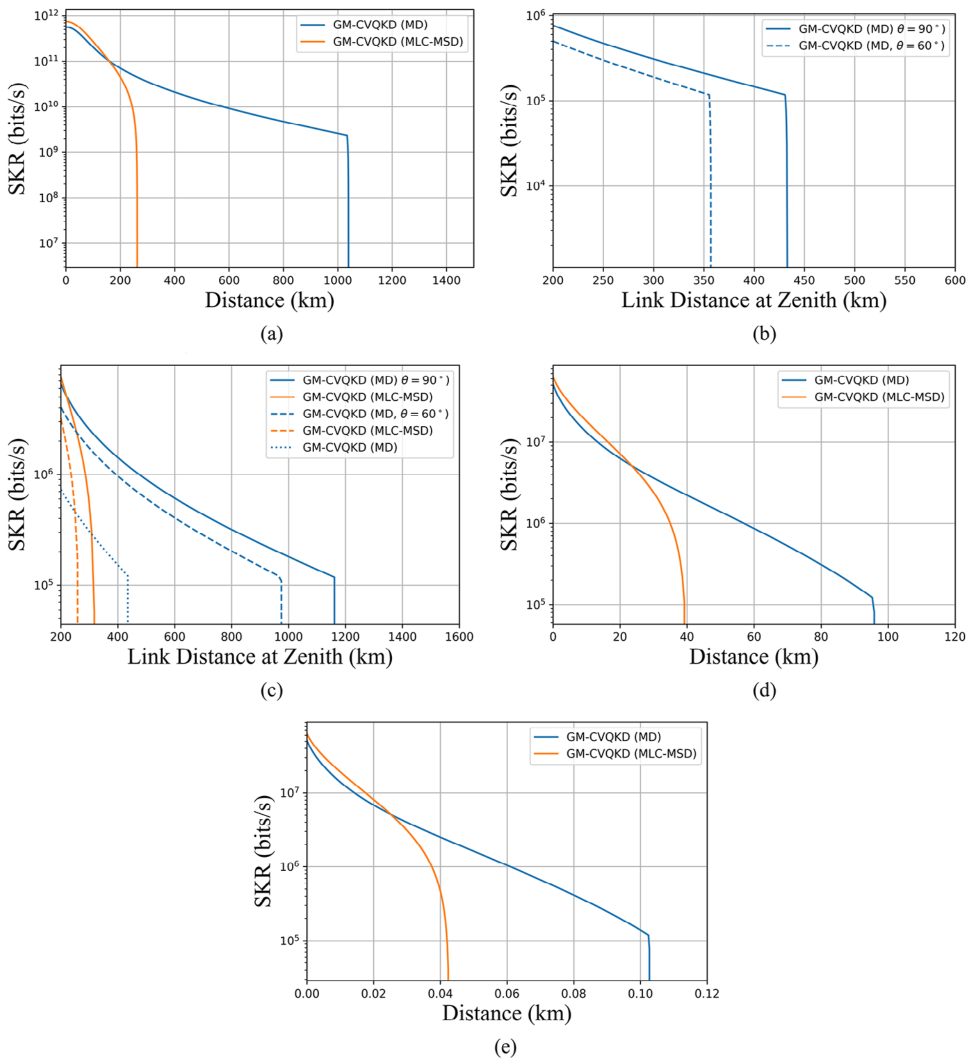

Figure A1. Finite size limit SKRs for GM-CVQKD using MD and MLC-MSD reconciliation in the different links studied: a) Inter-satellite, $r_a = w_0 = 0.2$ m; b) Uplink, $D_R = 0.3$ m, $D_T = 1$ m. Using MLC-MSD reconciliation did not produce positive SKRs; c) Downlink, $D_R = 1$ m, $D_T = 0.3$ m; d) Fiber-based; e) Underwater with pure sea water.

- Increasing the OGS elevation increases the maximum link distance and therefore satellite orbit altitude for which a positive SKR is possible. This results from the decrease in attenuation from a decrease in link distance and effective atmosphere thickness as Bob is effectively closer to Alice.
- Operating in atmospheric conditions where there is greater visibility, a smaller refractive index structure parameter (C_n^2), and smaller scintillation increases the overall link distance. This results from the decrease in attenuation due to less atmospheric scattering, turbulence, and beam wandering.

Inter-Satellite Links: The main parameters influencing inter-satellite links are the receiver aperture and the beam waist radius. Increasing these values leads to larger transmittances and therefore more positive and higher SKRs.

Underwater Links: The absorption and scattering coefficients are the main parameters which affect the transmittance in underwater links. These coefficients are influenced by the chlorophyll concentration in the water. Having a smaller concentration of chlorophyll leads to smaller absorption and scattering coefficients and consequently a larger transmittance that leads to more positive and larger SKRs.

Overall, the calculation and parameter analysis of SKRs show that inter-satellite links allow the longest link distances, followed by satellite-to-ground links, fiber links, and underwater links in descending order. Although inter-satellite links (**Figure A1a**) show smaller positive SKRs for slightly smaller distances than downlinks (Figure A1c), this is because smaller apertures were used in the calculation to represent typical aperture sizes in space. For the same sized apertures, inter-satellite links achieve larger positive SKRs for larger distances compared to satellite-to-ground links. It can also be seen that MD reconciliation outperforms MLC-MSD reconciliation by producing larger positive SKRs at larger link distances.

Acknowledgements

M. T. S. is a University of Auckland Doctoral Scholar. This research was supported by A*STAR under Project No. C230917009, and Q.InC Strategic Research and Translational Thrust.

Open access publishing facilitated by The University of Auckland, as part of the Wiley - The University of Auckland agreement via the Council of Australian University Librarians.

Conflict of Interest

The authors declare no conflict of interest.

Data Availability Statement

The data that support the findings of this study are available from the corresponding author upon reasonable request.

Keywords

network routing, quantum communications, quantum networks, quantum key distribution

Received: February 20, 2025
Revised: April 30, 2025
Published online: June 11, 2025

[1] C. Simon, *Nat. Photonics* **2017**, *11*, 678.
[2] F. Laudenbach, C. Pacher, C.-H. F. Fung, A. Poppe, M. Peev, B. Schrenk, M. Hentschel, P. Walther, H. Hübel, *Adv. Quantum Technol.* **2018**, *1*, 1800011.
[3] S. P. Kish, P. J. Gleeson, A. Walsh, P. K. Lam, S. M. Assad, *Quantum* **2024**, *8*, 1382.
[4] Y. Cao, Y. Zhao, Q. Wang, J. Zhang, S. X. Ng, L. Hanzo, *IEEE Commun. Surv. Tutor.* **2022**, *24*, 839.
[5] C. Elliott, *New J. Phys.* **2002**, *4*, 46.
[6] C. Elliott, A. Colvin, D. Pearson, O. Pikalo, J. Schlafer, H. Yeh, in *Quantum Information and Computation III*, vol. *5815*, SPIE, Bellingham, WA **2005**, pp. 138–149.
[7] M. Sasaki, M. Fujiwara, H. Ishizuka, W. Klaus, K. Wakui, M. Takeoka, S. Miki, T. Yamashita, Z. Wang, A. Tanaka, K. Yoshino, Y. Nambu, S. Takahashi, A. Tajima, A. Tomita, T. Domeki, T. Hasegawa, Y. Sakai, H. Kobayashi, T. Asai, K. Shimizu, T. Tokura, T. Tsurumaru, M. Matsui, T. Honjo, K. Tamaki, H. Takesue, Y. Tokura, J. F. Dynes, A. R. Dixon, et al., *Opt. Express* **2011**, *19*, 10387.
[8] M. Sasaki, M. Fujiwra, H. Ishizuka, W. Klaus, K. Wakui, M. Takeoka, A. Tanaka, K. Yoshino, Y. Nambu, S. Takahashi, A. Tajima, A. Tomita, T. Domeki, T. Hasegawa, Y. Sakai, H. Kobayashi, T. Asai, K. Shimizu, T. Tokura, T. Tsurumaru, M. Matsui, T. Honjo, K. Tamaki, H. Takesue, Y. Tokura, J. F. Dynes, A. Dixon, A. W. Sharpe, Z. L. Yuan, A. J. Shields, et al., in *CLEO:2011 - Laser Applications to Photonic Applications*, Optica Publishing Group, Washington **2011**, JTuC1.
[9] M. Dianati, R. Alléaume, in *2007 First International Conference on Quantum, Nano, and Micro Technologies (ICQNM'07)*, IEEE, Piscataway, NJ **2007**, pp. 13–13.
[10] M. Peev, C. Pacher, R. Alléaume, C. Barreiro, J. Bouda, W. Boxleitner, T. Debuisschert, E. Diamanti, M. Dianati, J. F. Dynes, S. Fasel, S. Fossier, M. Fürst, J.-D. Gautier, O. Gay, N. Gisin, P. Grangier, A. Happe, Y. Hasani, M. Hentschel, H. Hübel, G. Humer, T. Länger, M. Legrë, R. Lieger, J. Lodewyck, T. Lorünser, N. Lütkenhaus, A. Marhold, T. Matyus, et al., *New J. Phys.* **2009**, *11*, 075001.
[11] V. Martín, A. Aguado, J. P. Brito, A. Sanz, P. Salas, D. R. López, V. López, A. Pastor-Perales, A. Poppe, M. Peev, in *2019 21st International Conference on Transparent Optical Networks (ICTON)*, IEEE, Piscataway, NJ **2019**, pp. 1–4.
[12] M. I. García Cid, L. Ortiz Martín, V. Martín Ayuso, in *Proceedings of the 16th International Conference on Availability, Reliability and Security*, **2021**, pp. 1–7, ACM Digital Library: https://dl.acm.org/doi/abs/10.1145/3465481.3470056.
[13] V. Martin, J. P. Brito, L. Ortíz, R. B. Méndez, J. S. Buruaga, R. J. Vicente, A. Sebastián-Lombraña, D. Rincón, F. Pérez, C. Sánchez, M. Peev, H. Brunner, F. Fung, A. Poppe, F. Fröwis, A. J. Shields, R. I. Woodward, H. Griesser, S. Roehrich, F. de la Iglesia, C. Abellán, M. Hentschel, J. M. Rivas-Moscoso, A. Pastor-Perales, J. Folgueira, D. López, *npj Quantum Inf.* **2024**, *10*, 80.
[14] H. Wang, Y. Zhao, A. Nag, *Appl. Sci.* **2019**, *9*, 2081.
[15] Y.-A. Chen, Q. Zhang, T.-Y. Chen, W.-Q. Cai, S.-K. Liao, J. Zhang, K. Chen, J. Yin, J.-G. Ren, Z. Chen, S.-L. Han, Q. Yu, K. Liang, F. Zhou, X. Yuan, M.-S. Zhao, T.-Y. Wang, X. Jiang, L. Zhang, W.-Y. Liu, Y. Li, Q. Shen, Y. Cao, C.-Y. Lu, R. Shu, J.-Y. Wang, L. Li, N.-L. Liu, F. Xu, X.-B. Wang, et al., *Nature* **2021**, *589*, 214.
[16] S.-K. Liao, W.-Q. Cai, J. Handsteiner, B. Liu, J. Yin, L. Zhang, D. Rauch, M. Fink, J.-G. Ren, W.-Y. Liu, Y. Li, Q. Shen, Y. Cao, F.-Z. Li, J.-F. Wang, Y.-M. Huang, L. Deng, T. Xi, L. Ma, T. Hu, L. Li, N.-L. Liu, F. Koidl, P. Wang, Y.-A. Chen, X.-B. Wang, M. Steindorfer, G. Kirchner, C.-Y. Lu, R. Shu, et al., *Phys. Rev. Lett.* **2018**, *120*, 030501.
[17] X. Su, W. Wang, Y. Wang, X. Jia, C. Xie, K. Peng, *Europhys. Lett.* **2009**, *87*, 20005.
[18] S. Ren, Y. Wang, X. Su, *Sci. China Inf. Sci.* **2022**, *65*, 200502.
[19] J. Dynes, A. Wonfor, W.-S. Tam, A. Sharpe, R. Takahashi, M. Lucamarini, A. Plews, Z. Yuan, A. Dixon, J. Cho, Y. Tanizawa, J. P. Elbers, H. Greißer, I. H. White, R. V. Penty, A. J. Shields, *npj Quantum Inf.* **2019**, *5*, 101.
[20] R. S. Tessinari, A. Bravalheri, E. Hugues-Salas, R. Collins, D. Aktas, R. S. Guimaraes, O. Alia, J. Rarity, G. T. Kanellos, R. Nejabati, D. Simeonidou, in *45th European Conference on Optical Communication (ECOC 2019)*, **2019**, pp. 1–4, https://ieeexplore.ieee.org/abstract/document/9125761.
[21] S. K. Joshi, D. Aktas, S. Wengerowsky, M. Lončarić, S. P. Neumann, B. Liu, T. Scheidl, G. C. Lorenzo, Željko Samec, L. Kling, A. Qiu, M. Razavi, M. Stipčević, J. G. Rarity, R. Ursin, *Sci. Adv.* **2020**, *6*, eaba0959.
[22] S. Mishra, A. Biswas, S. Patil, P. Chandravanshi, V. Mongia, T. Sharma, A. Rani, S. Prabhakar, S. Ramachandran, R. P. Singh, *J. Opt.* **2022**, *24*, 074002.
[23] J. S. Sidhu, S. K. Joshi, M. Gündoğan, T. Brougham, D. Lowndes, L. Mazzarella, M. Krutzik, S. Mohapatra, D. Dequal, G. Vallone, P. Villoresi, A. Ling, T. Jennewein, M. Mohageg, J. G. Rarity, I. Fuentes, S. Pirandola, D. K. L. Oi, *IET Quantum Comm.* **2021**, *2*, 182.
[24] N. J. Rattenbury, J. Ashby, F. Bennet, M. Birch, J. E. Cater, K. Ferguson, D. Giggenbach, K. Grant, A. Knopp, M. T. Knopp, E. Kruzins, A. Lambert, K. Mudge, C. Qualtrough, S. Raffa, J. Rittershofer, M. Sayat, S. Schediwy, R. T. Schwarz, M. Sellars, O. Thearle, T. Travouillon, K. Walker, S. Walsh, S. Weddell, *arXiv preprint arXiv:2402.13282* **2024**.
[25] M. Sayat, S. P. Kish, P. K. Lam, N. Rattenbury, J. Cater, in *Quantum Computing, Communication, and Simulation IV*, (Eds.: P. R. Hemmer, A. L. Migdall), vol. *12911*, International Society for Optics and Photonics, SPIE, Bellingham, WA **2024**, pp. 97–111.
[26] W. Maeda, A. Tanaka, S. Takahashi, A. Tajima, A. Tomita, *IEEE J. Sel. Top. Quantum Electron.* **2009**, *15*, 1591.
[27] Y. Cao, Y. Zhao, C. Colman-Meixner, X. Yu, J. Zhang, *Opt. Express* **2017**, *25*, 26453.
[28] Y. Cao, Y. Zhao, X. Yu, Y. Wu, *J. Opt. Comm. Netw.* **2017**, *9*, 995.
[29] A. Tajima, T. Kondoh, T. Ochi, M. Fujiwara, K. Yoshino, H. Iizuka, T. Sakamoto, A. Tomita, E. Shimamura, S. Asami, M. Sasaki, *Quantum Sci. Technol.* **2017**, *2*, 034003.
[30] Y. Zhao, Y. Cao, W. Wang, H. Wang, X. Yu, J. Zhang, M. Tornatore, Y. Wu, B. Mukherjee, *IEEE Commun. Mag.* **2018**, *56*, 130.
[31] Y. Cao, Y. Zhao, J. Wang, X. Yu, Z. Ma, J. Zhang, *IEEE Commun. Mag.* **2019**, *57*, 152.
[32] ITU-T, *Itu-T* **2019**, 22, https://www.itu.int/rec/T-REC-Y.3800-201910-I/en.
[33] C. Elliot, H. Yeh, *BBN Technologies* **2007**, https://apps.dtic.mil/sti/tr/pdf/ADA471450.pdf.
[34] A. Leverrier, P. Grangier, *Phys. Rev. Lett.* **2009**, *102*, 180504.
[35] A. Denys, P. Brown, A. Leverrier, *Quantum* **2021**, *5*, 540.

[36] M. T. Sayat, O. Thearle, B. Shajilal, S. P. Kish, P. K. Lam, N. J. Rattenbury, J. E. Cater, *Entropy* **2024**, *26*, 865.
[37] T. Matsuura, K. Maeda, T. Sasaki, M. Koashi, *Nat. Commun.* **2021**, *12*, 252.
[38] S. Yamano, T. Matsuura, Y. Kuramochi, T. Sasaki, M. Koashi, *Phys. Scr.* **2024**, *99*, 025115.
[39] F. Kanitschar, I. George, J. Lin, T. Upadhyaya, N. Lütkenhaus, *PRX Quantum* **2023**, *4*, 040306.
[40] H. Mani, T. Gehring, P. Grabenweger, B. Ömer, C. Pacher, U. L. Andersen, *Phys. Rev. A* **2021**, *103*, 062419.
[41] R. Mueller, D. Ribezzo, M. Zahidy, L. K. Oxenløwe, D. Bacco, S. Forchhammer, *Quantum Inf. Process.* **2024**, *23*, 195.
[42] S. J. Johnson, A. M. Lance, L. Ong, M. Shirvanimoghaddam, T. Ralph, T. Symul, *New J. Phys.* **2017**, *19*, 023003.
[43] S. Jeong, H. Jung, J. Ha, *npj Quantum Inf.* **2022**, *8*, 6.
[44] M. T. Sayat, B. Shajilal, S. P. Kish, S. M. Assad, T. Symul, P. K. Lam, N. J. Rattenbury, J. E. Cater, *IEEE Trans. Commun.* **2024**, *72*, 3244.
[45] S. P. Kish, E. Villaseñor, R. Malaney, K. A. Mudge, K. J. Grant, *Quantum Eng.* **2020**, *2*, e50.
[46] N. Hosseinidehaj, A. M. Lance, T. Symul, N. Walk, T. C. Ralph, *Phys. Rev. A* **2020**, *101*, 052335.
[47] A. Leverrier, *Phys. Rev. Lett.* **2015**, *114*, 070501.
[48] C. Lupo, C. Ottaviani, P. Papanastasiou, S. Pirandola, *Phys. Rev. A* **2018**, *97*, 052327.
[49] S. Pirandola, *Phys. Rev. Res.* **2021**, *3*, 013279.
[50] S. Pirandola, *Phys. Rev. Res.* **2021**, *3*, 023130.
[51] H. Wang, Y. Pi, Y. Shao, Y. Pan, W. Huang, Y. Li, B. Xu, in *2021 19th International Conference on Optical Communications and Networks (ICOCN)*, IEEE, Piscataway, NJ **2021**, pp. 1–3.
[52] T. Hirano, T. Ichikawa, T. Matsubara, M. Ono, Y. Oguri, R. Namiki, K. Kasai, R. Matsumoto, T. Tsurumaru, *Quantum Sci. Technol.* **2017**, *2*, 024010.
[53] D. Huang, J. Fang, C. Wang, P. Huang, G.-H. Zeng, *Chin. Phys. Lett.* **2013**, *30*, 114209.
[54] S. Ren, S. Yang, A. Wonfor, I. White, R. Penty, *Sci. Rep.* **2021**, *11*, 9454.
[55] Y. Zhang, Z. Chen, S. Pirandola, X. Wang, C. Zhou, B. Chu, Y. Zhao, B. Xu, S. Yu, H. Guo, *Phys. Rev. Lett.* **2020**, *125*, 010502.
[56] A. A. E. Hajomer, I. Derkach, N. Jain, H.-M. Chin, U. L. Andersen, T. Gehring, *Sci. Adv.* **2024**, *10*, eadi9474.
[57] N. Hosseinidehaj, Z. Babar, R. Malaney, S. X. Ng, L. Hanzo, *IEEE Comm. Surv. Tutor.* **2018**, *21*, 881.
[58] W. Zhao, R. Shi, X. Ruan, Y. Guo, Y. Mao, Y. Feng, *Quantum Inf. Process.* **2022**, *21*, 186.
[59] C. Gabriel, M.-A. Khalighi, S. Bourennane, P. Leon, V. Rigaud, in *2011 IEEE GLOBECOM Workshops (GC Wkshps)*, IEEE, Piscataway, NJ **2011**, pp. 833–837.
[60] R. M. Kraemer, L. M. Pessoa, H. M. Salgado, in *Wireless Mesh Networks-Security, Architectures and Protocols*, IntechOpen, London **2019**.
[61] J. Xu, Y. Song, X. Yu, A. Lin, M. Kong, J. Han, N. Deng, *Opt. Express* **2016**, *24*, 8097.
[62] M. Kong, J. Wang, Y. Chen, T. Ali, R. Sarwar, Y. Qiu, S. Wang, J. Han, J. Xu, *Opt. Express* **2017**, *25*, 21509.
[63] A. Morel, L. Prieur, *Limnol. oceanogr.* **1977**, *22*, 709.
[64] L. Prieur, S. Sathyendranath, *Limnol. oceanogr.* **1981**, *26*, 671.
[65] T. E. S. Agency, Types of orbits, https://www.esa.int/Enabling_Support/Space_Transportation/Types_of_orbits.
[66] C. Liu, C. Zhu, M. Nie, H. Yang, C. Pei, *Opt. Express* **2022**, *30*, 14798.
[67] C. Liorni, H. Kampermann, D. Bruß, *New J. Phys.* **2019**, *21*, 093055.
[68] Z. Zuo, Y. Wang, D. Huang, Y. Guo, *J. Phys. A: Mathematical and Theoretical* **2020**, *53*, 465302.
[69] M. Aspelmeyer, T. Jennewein, M. Pfennigbauer, W. R. Leeb, A. Zeilinger, *IEEE J. Sel. Top. Quantum Electron.* **2003**, *9*, 1541.
[70] J. Bourgoin, E. Meyer-Scott, B. L. Higgins, B. Helou, C. Erven, H. Huebel, B. Kumar, D. Hudson, I. D'Souza, R. Girard, R. Laflamme, T. Jennewein, *New J. Phys.* **2013**, *15*, 023006.
[71] R. Bedington, J. M. Arrazola, A. Ling, *npj Quantum Inf.* **2017**, *3*, 30.
[72] L. C. Andrews, R. L. Phillips, C. Y. Young, *Opt. Eng.* **2000**, *39*, 3272.
[73] A. M. Aly, H. A. Fayed, N. E. Ismail, M. H. Aly, *Opt. Quantum Electron.* **2020**, *52*, 1.
[74] I. I. Kim, B. McArthur, E. J. Korevaar, in *Optical Wireless Communications III*, vol. *4214*, SPIE, Bellingham, WA **2001**, pp. 26–37.
[75] M. Grabner, V. Kvicera, in *2010 Loughborough Antennas & Propagation Conference*, IEEE, Piscataway, NJ **2010**, pp. 193–196.
[76] D. Giggenbach, H. Henniger, *Opt. Eng.* **2008**, *47*, 046001.
[77] L. C. Andrews, R. L. Phillips, D. Wayne, T. Leclerc, P. Sauer, R. Crabbs, J. Kiriazes, in *Atmospheric Propagation VI*, vol. *7324*, SPIE, Bellingham, WA **2009**, pp. 11–22.
[78] S. S. Muhammad, P. Kohldorfer, E. Leitgeb, in *Proceedings of 2005 7th International Conference Transparent Optical Networks, 2005*, vol *1*, IEEE, Piscataway, NJ **2005**, pp. 407–410.
[79] F. Dios, J. A. Rubio, A. Rodríguez, A. Comeron, *Appl. Opt.* **2004**, *43*, 3866.
[80] A. Csete, Gpredict, http://gpredict.oz9aec.net/.
[81] O. Kegege, M. Fuentes, N. Meyer, A. Sil, in *2012 IEEE Aerospace Conference*, IEEE, Piscataway, NJ **2012**, pp. 1–9.
[82] F. Bennet, K. Ferguson, K. Grant, E. Kruzins, N. Rattenbury, S. Schediwy, in *Free-Space Laser Communications XXXII*, vol. *11272*, SPIE, Bellingham, WA **2020**, p. 1127202.
[83] N. Gupta, K. Mangla, A. K. Jha, M. Umar, *Int. J. New Technol. Res.* **2016**, *2*, 122.
[84] Z. Chen, X. Wang, S. Yu, Z. Li, H. Guo, *npj Quantum Inf.* **2023**, *9*, 28.
[85] C.-Y. Lu, Y. Cao, C.-Z. Peng, J.-W. Pan, *Rev. Mod. Phys.* **2022**, *94*, 035001.
[86] F. Furrer, W. J. Munro, *Phys. Rev. A* **2018**, *98*, 032335.
[87] J. Dias, M. S. Winnel, N. Hosseinidehaj, T. C. Ralph, *Phys. Rev. A* **2020**, *102*, 052425.
[88] A. Gupta, et al., *Procedia Comput. Sci.* **2016**, *89*, 99.
[89] Y. Wang, H. Xu, D. Li, R. Wang, C. Jin, X. Yin, S. Gao, Q. Mu, L. Xuan, Z. Cao, *Sci. Rep.* **2018**, *8*, 1124.
[90] V. W. Chan, *J. Lightwave Technol.* **2006**, *24*, 4750.
[91] Y. Tanizawa, R. Takahashi, A. R. Dixon, in *2016 Eighth International Conference on Ubiquitous and Future Networks (ICUFN)*, IEEE, Piscataway, NJ **2016**, pp. 208–214.
[92] I. B. Djordjevic, *Phys.-Layer Sec. Quantum Key Distr.* **2019**, 211.
[93] W.-B. Liu, C.-L. Li, Y.-M. Xie, C.-X. Weng, J. Gu, X.-Y. Cao, Y.-S. Lu, B.-H. Li, H.-L. Yin, Z.-B. Chen, *PRX Quantum* **2021**, *2*, 040334.
[94] H.-K. Lo, Y. Zhao, *arXiv preprint arXiv:0803.2507* **2008**.
[95] Q. Ruihong, M. Ying, *J. Phys.: Conference Series* **2019**, *1237*, 052032.
[96] A. Conrad, S. Isaac, R. Cochran, D. Sanchez-Rosales, B. Wilens, A. Gutha, T. Rezaei, D. J. Gauthier, P. Kwiat, in *Free-space laser communications XXXIII*, vol. *11678*, SPIE, Bellingham, WA **2021**, pp. 177–184.
[97] C. Fuchs, M. Brechtelsbauer, J. Horwath, A. Shrestha, F. Moll, D. Giggenbach, C. Schmidt, in *Advanced Solid-State Lasers Congress*, Optica Publishing Group, Washington **2013**, pp. LTu1B.3.